



PAPER

Shear wave propagation in viscoelastic media: validation of an approximate forward model

Fernando Zvietcovich¹, Natalie Baddour², Jannick P Rolland³ and Kevin J Parker^{1,4}¹ Department of Electrical and Computer Engineering, University of Rochester, Hopeman Building 203, PO Box 270126, Rochester, NY 14627-0126, United States of America² Department of Mechanical Engineering, University of Ottawa, Ontario, Canada³ The Institute of Optics, University of Rochester, Rochester, NY 14627-0186, United States of America⁴ Author to whom any correspondence should be addressed.E-mail: kevin.parker@rochester.edu**Keywords:** shear wave propagation, axisymmetric Gaussian force, attenuation, dispersion, viscoelastic models, tissues, elastography**Abstract**

Many approaches to elastography incorporate shear waves; in some systems these are produced by acoustic radiation force (ARF) push pulses. Understanding the shape and decay of propagating shear waves in lossy tissues is key to obtaining accurate estimates of tissue properties, and so analytical models have been proposed. In this paper, we reconsider a previous analytical model with the goal of obtaining a computationally straightforward and efficient equation for the propagation of shear waves from a focal push pulse. Next, this model is compared with an experimental optical coherence tomography (OCT) system and with finite element models, in two viscoelastic materials that mimic tissue. We find that the three different cases—analytical model, finite element model, and experimental results—demonstrate reasonable agreement within the subtle differences present in their respective conditions. These results support the use of an efficient form of the Hankel transform for both lossless (elastic) and lossy (viscoelastic) media, and for both short (impulsive) and longer (extended) push pulses that can model a range of experimental conditions.

1. Introduction

Within the broad field of elastography (Ophir *et al* 2011, Parker *et al* 2011), one approach to generating shear waves in tissues utilizes a push pulse of acoustic radiation force (ARF) from a focused ultrasound transducer (Sarvazyan *et al* 1998). The resulting disturbance can be tracked using motion detection techniques implemented in different imaging systems, such as ultrasound and optical coherence tomography (OCT), and, from these waveforms, parameters including shear wave speed are extracted. Accurate analytical models can be helpful in understanding the phenomenon of how the shear waves evolve over space and time in tissues. A number of analytical models have been proposed (Sarvazyan *et al* 1998, Nightingale *et al* 1999, Bercoff *et al* 2004, Fahey *et al* 2005, Vappou *et al* 2009, Schmitt *et al* 2010, Parker and Baddour 2014, Wijesinghe *et al* 2015, Kazemirad *et al* 2016, Leartprapun *et al* 2017, Nenadic *et al* 2017) to capture the evolution of shear waves from a push pulse, under a range of conditions and assumptions relevant to clinical elastography.

Herein, we focus on the specific case of a rotationally symmetric push pulse that is long in the axial direction, leading to solutions in cylindrical coordinates. A prior set of derivations was proposed by Parker and Baddour (2014) with additional experimental and theoretical developments (Zvietcovich *et al* 2017a, Baddour 2018, Parker *et al* 2018) published more recently. However, a number of issues remain and are the subject of this paper. First, within the possible uses of Baddour's Integral Theorems (Baddour 2011), we examine which strategy leads to the more straightforward solutions including numerical solutions. In this case, we choose a path that avoids the singularities and other issues associated with the complex Hankel functions in favor of a path leading to a simpler Bessel function integrand, commensurate with Hankel transform interpretation. Second, we apply these techniques to two phantom materials with lower and higher viscoelastic loss parameters to predict the propagating shear wave pulses from an applied push pulse. These predictions are compared with experimental OCT data

and with finite element analysis results. The three approaches produce similar results and confirm the utility of our analytical model within reasonable experimental parameters.

The paper is organized as follows: first, in section 2, we review the theory of axisymmetric propagating shear wave pulses in elastic and then in viscoelastic materials. Subsequently, in section 3, we describe the methodology for selecting phantom materials mimicking lossless and lossy conditions and the viscoelastic characterization using mechanical testing analysis. This section also includes: the description of wave propagation experiments (EXP) in those phantoms using an OCT system and an ARF ultrasonic transducer all implemented in an integrated setup; details on the simulation of wave propagation under the same material properties and boundary conditions using finite elements (FE); and the predictions of our proposed model in the same context. In section 4, results are shown and compared for the following cases: OCT EXP, finite element models, and our model predictions. The utility of our model, its extension under the assumptions made, and limitations are discussed in section 5. Finally, conclusions of the entire work are summarized in section 6.

2. Theory

2.1. Cylindrical shear wave equation produced by a body force excitation

The governing equation describing the motion produced by a propagating shear horizontal wave in a homogeneous, isotropic and elastic material, using the notation from Graff (1975) in cylindrical coordinates, is given as

$$\nabla^2 u_z(r, \theta, z; t) - \frac{1}{c^2} \frac{\partial^2 u_z(r, \theta, z; t)}{\partial t^2} = -\frac{1}{c^2} F_z(r, \theta, z) g(t), \quad (1)$$

where ∇^2 is the Laplacian operator in cylindrical coordinates, $u_z(r, \theta, z; t)$ is the displacement of the shear wave in the z -direction, c is the velocity of the wave; $F_z(r, \theta, z)$ is the distribution of the applied body force in the z -direction, and $g(t)$ is the temporal application of the force. We assume that, given the direction of the applied force, the produced shear wave will propagate cylindrically outwards from the source origin, parallel to the $\widehat{r\theta}$ -plane. Therefore, the displacement is polarized in the z -direction, and any derivatives of u_z with respect to θ or z are zero.

The force source $F_z(r, \theta, z)$ is assumed to be axisymmetric and extended uniformly in the z -direction, similar to most of the ultrasound (US)-based ARF excitation beams. Figure 1 shows a Gaussian-shaped force produced by a spherically focused US transducer located at the origin of a polar coordinate system, and described as

$$F_z(r, \theta, z) = A_0 \left(\frac{1}{2\sigma^2} \right) e^{-\left(\frac{r}{2\sigma}\right)^2}, \quad (2)$$

where σ^2 is the half variance of the pulse shape, and A_0 is the force intensity.

Introducing the displacement and source constraints, and assuming displacement and particle velocity are set to zero everywhere as initial conditions, equation (1) can be rewritten as

$$\nabla^2 u_z(r, t) - \frac{1}{c^2} \frac{\partial^2 u_z(r, t)}{\partial t^2} = -\frac{1}{c^2} F_z(r)g(t). \quad (3)$$

The shear speed c in equation (3) is related to the shear modulus μ of an elastic, homogenous, and incompressible medium with a density ρ as $c = \sqrt{\mu/\rho}$. However, in a viscoelastic medium, the shear modulus is a complex and frequency-dependent quantity $\widehat{\mu}(\omega) = \mu_s(\omega) + i\mu_l(\omega)$, where $\mu_s(\omega)$ and $\mu_l(\omega)$ are called the shear storage and loss moduli, respectively (Carstensen *et al* 2014). Then, $\widehat{c}(\omega) = \sqrt{\widehat{\mu}(\omega)/\rho}$, and the wave equation is better represented in the Fourier domain. Taking the temporal Fourier transform \mathfrak{F} of equation (3), yields

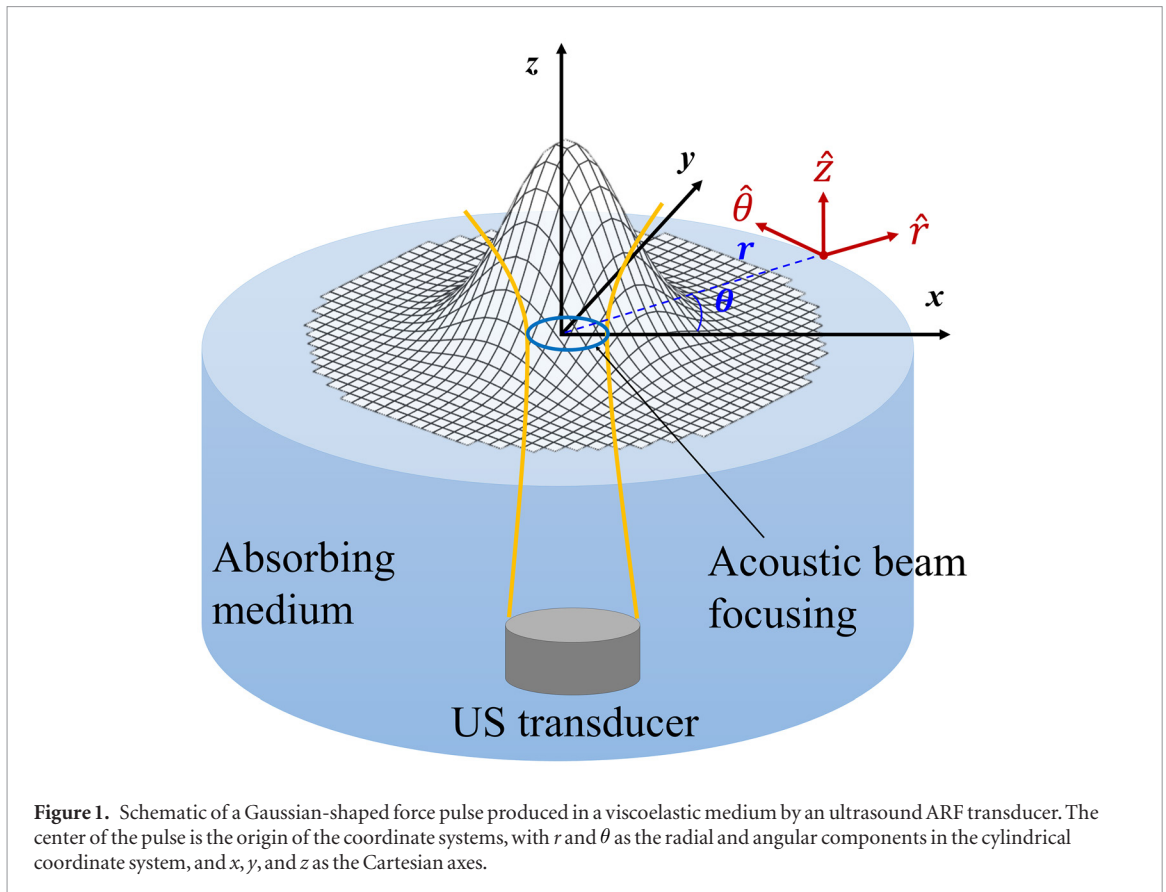
$$\nabla^2 U_z(r, \omega) + \widehat{k}(\omega)^2 U_z(r, \omega) = -\frac{1}{\widehat{c}(\omega)^2} F_z(r)G(\omega), \quad (4)$$

where $U_z(r, \omega) = \mathfrak{F}\{u_z(r, t)\}$, \widehat{k} is the complex wave number $\widehat{k}(\omega) = \omega/\widehat{c}(\omega)$, $G(\omega) = \mathfrak{F}\{g(t)\}$, and ω is the angular frequency with respect to time.

2.2. Cylindrical coordinate solution: green's function in an elastic medium

The Laplacian operator in equation (3) for cylindrical coordinates leads naturally to the Hankel transform (Graff 1975). Thus, applying the zeroth order Hankel transform \mathcal{H}_0 in space to equation (4) in cylindrical coordinates yields:

$$\widehat{U}_z(\varepsilon, \omega) = \frac{1}{c^2} \frac{\widehat{F}(\varepsilon)G(\omega)}{\varepsilon^2 - \frac{\omega^2}{c^2}} \quad (5)$$



where $\widehat{F}(\varepsilon) = \mathcal{H}_0\{F_z(r)\}$, ε is the spatial frequency, $G(\omega) = \mathfrak{F}\{g(t)\}$, $\widehat{U}_z(\varepsilon, \omega) = \mathfrak{F}\{\mathcal{H}\{u_z(r, t)\}(\varepsilon, t)\}$, and where we assume convergence of the transform integrals under well-behaved and realizable functions. Applying the inverse Hankel transform to $\widehat{U}_z(\varepsilon, \omega)$, we obtain:

$$U_z(r, \omega) = \frac{1}{c^2} \int_0^\infty \frac{\widehat{F}(\varepsilon) \cdot G(\omega)}{\varepsilon^2 - \frac{\omega^2}{c^2}} J_0(\varepsilon r) \varepsilon d\varepsilon. \quad (6)$$

Alternatively, if we apply the inverse Fourier transform to $\widehat{U}_z(\varepsilon, \omega)$, we obtain:

$$\widehat{u}_z(\varepsilon, t) = \frac{1}{2\pi c^2} \int_{-\infty}^\infty \frac{\widehat{F}(\varepsilon) G(\omega)}{\varepsilon^2 - \frac{\omega^2}{c^2}} e^{+i\omega t} d\omega \quad (7)$$

where $G(\omega)$ is the temporal Fourier transform of any arbitrary shape of $g(t)$. Thus,

$$\widehat{u}_z(\varepsilon, t) = \frac{\widehat{F}(\varepsilon)}{2\pi} \int_{-\infty}^\infty \frac{G(\omega)}{c^2 \varepsilon^2 - \omega^2} e^{+i\omega t} d\omega \quad (8)$$

for $\varepsilon \geq 0$. Now, applying Baddour's Theorem 5 of Baddour (2011):

$$\widehat{u}_z(\varepsilon, t) = \frac{i\widehat{F}(\varepsilon)}{2} \left[\frac{G(-c\varepsilon)e^{-ic\varepsilon t}}{c\varepsilon} \right] \quad (9)$$

for $\varepsilon \geq 0$, and $t > 0$. Then, assuming $g(t)$ is real, so $G(-c\varepsilon) = G^*(c\varepsilon)$, and evaluating particle velocity:

$$\widehat{v}_z(\varepsilon, t) = \frac{d}{dt} [\widehat{u}_z(\varepsilon, t)] = \frac{\widehat{F}(\varepsilon)}{2} [G^*(c\varepsilon)e^{-ic\varepsilon t}] \quad (10)$$

for $\varepsilon \geq 0$, and $t > 0$. Now, taking the inverse Hankel transform

$$v_z(r, t) = \frac{1}{2} \int_0^\infty \varepsilon \cdot \widehat{F}(\varepsilon) G^*(c\varepsilon) \cdot J_0(\varepsilon r) e^{-ic\varepsilon t} d\varepsilon \quad (11)$$

for $\varepsilon \geq 0$, $r \geq 0$, and $t > 0$. Assuming $g(t) = \delta(t)$ is a temporal impulse, then $G^*(\omega) = 1$. Furthermore, from a real intensity pattern $F_z(r)$, we have $\widehat{F}(\varepsilon)$ as a real function. Then, we select the real part of equation (11) as the physical component of the wave for $r \geq 0$ and $t > 0$, yielding

$$v_z(r, t) = \frac{1}{2} \int_0^\infty \varepsilon \cdot \widehat{F}(\varepsilon) \cdot J_0(\varepsilon r) \cos(c\varepsilon t) d\varepsilon \quad (12)$$

for $\varepsilon \geq 0, r \geq 0$, and $t > 0$. Let us assume, for instance, that $F_z(r)$ is a Gaussian-shaped force given by equation (2), then $\widehat{F}(\varepsilon) = A_0 e^{-(\sigma\varepsilon)^2}$. Then, following Chapter 5 of Graff (1975), the constant A_0 is scaled by $2c^2$ and we obtain:

$$v_z(r, t) = c^2 \int_0^\infty \varepsilon \cdot e^{-\sigma^2\varepsilon^2} \cdot J_0(\varepsilon r) \cos(c\varepsilon t) d\varepsilon. \quad (13)$$

Comparing equation (13) with results from equation (31) in Parker and Baddour (2014) for the same situation:

$$v_z(r, t) = \int_0^\infty \omega \cdot e^{-\sigma^2(\frac{\omega}{c})^2} \cdot J_0(\frac{\omega}{c} \cdot r) \cos(\omega t) d\omega \quad (14)$$

which appears identical with the substitution of ε for ω/c . This route of derivation (equations (5)–(14)) places simpler interpretations on the functions without the complexities of applying Hermitian properties and causality to the complex Green's function $H_0^{(2)}[(\omega/c) \cdot r]$, a complex Hankel function of the second kind, which contains a singularity at the origin.

Since we used $g(t) = \delta(t)$, equation (13) is then the temporal impulse response of the system for a Gaussian-shaped beam pattern. Then, the time domain response for an extended push pulse $g(t)$ can be obtained simply by the time domain convolution equation:

$$v_e(r, t) = \int_0^\infty g(\tau) v_i(r, t - \tau) d\tau \quad (15)$$

for $r \geq 0$ and $t > 0$, v_e represents the response to an extended push and v_i the impulse response obtained from equation (13).

2.3. Green's function in a lossy medium

In this case, we examine the conventional approach where the complex wave number \widehat{k} is defined as:

$$\widehat{k} = \beta(\omega) - i\alpha(\omega) = \frac{\omega}{c_p(\omega)} - i\alpha(\omega) \quad (16)$$

where $c_p(\omega)$ is the phase velocity, $\alpha(\omega)$ the attenuation, and the frequency dependence of both is dispersive and linked by the Kramers–Kronig equations (Szabo 1995). Assuming small dispersion such that $c_p(\omega) \cong c_0$, where c_0 is a constant real speed value with dimensionality of m s^{-1} , and using the first order Taylor approximation of attenuation such that $\alpha(\omega) \cong \omega\alpha_1$, where α_1 dimensionality is in $(\text{Np/m})/(\text{rad/s})$, equation (16) becomes

$$\widehat{k} \approx \frac{\omega}{c_0} - i\omega\alpha_1. \quad (17)$$

Following the notation of equation (4), the complex wave number in a viscoelastic medium is defined as $\widehat{k}(\omega) = \omega/\widehat{c}(\omega)$, where $\widehat{c}(\omega)$ is the complex speed. Then, using equation (17), we find

$$\widehat{c} = \frac{c_0}{1 - ic_0\alpha_1} \approx c_0(1 + ic_0\alpha_1) = c_0 + ic_0^2\alpha_1. \quad (18)$$

Taking the Hankel transform of equation (4) for the viscoelastic case, we obtain:

$$\widehat{U}_z(\varepsilon, \omega) = \frac{\widehat{F}(\varepsilon)G(\omega)}{(\widehat{c}\varepsilon)^2 - \omega^2} \quad (19)$$

where $\widehat{F}(\varepsilon) = \mathcal{H}_0\{F_z(r)\}$, ε is the spatial frequency, and $\widehat{U}_z(\varepsilon, \omega) = \Im\{\mathcal{H}_0\{u_z(r, t)\}(\varepsilon, t)\}$. Applying the inverse Fourier Transform to equation (19), we obtain:

$$\widehat{u}_z(\varepsilon, t) = \frac{1}{2\pi} \int_{-\infty}^\infty \frac{\widehat{F}(\varepsilon)G(\omega)}{(\widehat{c}\varepsilon)^2 - \omega^2} e^{+i\omega t} d\omega. \quad (20)$$

From Baddour's Theorem 6 (Baddour 2011) for complex wave number with positive real part, and solving for $t > 0$, we have

$$\widehat{u}_z(\varepsilon, t) = -\frac{i}{2} \left[\frac{\widehat{F}(\varepsilon)G(\widehat{c}\varepsilon)e^{+i\widehat{c}\varepsilon t}}{\widehat{c}\varepsilon} \right]. \quad (21)$$

Applying the temporal derivative to equation (21) in order to calculate particle velocity, and replacing \widehat{c} with equation (18), we obtain

Table 1. Mechanical testing results in phantom materials M1 and M2. KVFD parameters (left col.) and complex wave number parameters (right col.) are shown for both materials. For all cases, $\rho = 1 \text{ g cm}^{-3}$ and incompressibility was assumed. All EXP were performed at room temperature (25 °C).

	Stress relaxation test: KVFD model parameters			Complex wave number: $\hat{k} = \frac{\omega}{c_0} - i\omega\alpha_1$	
	E_0 (kPa)	η (kPa s $^\alpha$)	τ	c_0 (m s $^{-1}$)	α_1 ($\frac{\text{NP}}{\text{m}}$ /rad)
M1	0.711 \pm 0.481	5.203 \pm 0.852	0.178 \pm 0.028	2.88 \pm 0.03	0.049 \pm 0.001
M2	9.969 \pm 9.661	24.928 \pm 12.217	0.086 \pm 0.025	4.61 \pm 0.02	0.009 \pm 0.002

$$\hat{v}_z(\varepsilon, t) = \frac{1}{2} \left[\hat{F}(\varepsilon) G(\hat{c}\varepsilon) \right] e^{+i c_0 \varepsilon t} \cdot e^{-\varepsilon c_0^2 \alpha_1 t}. \quad (22)$$

Defining $F_z(r)$ as a Gaussian-shaped force given by equation (2), and $g(t) = \delta(t)$ as a temporal impulse, then $\hat{F}(\varepsilon) G(\omega) = A_0 e^{-(\sigma\varepsilon)^2}$. After applying the inverse Hankel transform on the real part of equation (22), we obtain:

$$v_z(r, t) = \frac{A_0}{2} \int_0^\infty \varepsilon \cdot e^{-\sigma^2 \varepsilon^2} \cdot J_0(\varepsilon r) \cos(c_0 \varepsilon t) e^{-\varepsilon c_0^2 \alpha_1 t} d\varepsilon \quad (23)$$

which is an attenuated version of equation (13), under small dispersion, and weak attenuation assumptions. We note as well that equation (23) is consistent with equation (45) of Parker and Baddour (2014), under the weak dispersion assumption, despite the different approach taken therein to the solution. That comparison is made in more detail in appendix A.

3. Methods

3.1. Sample preparation and mechanical measurements

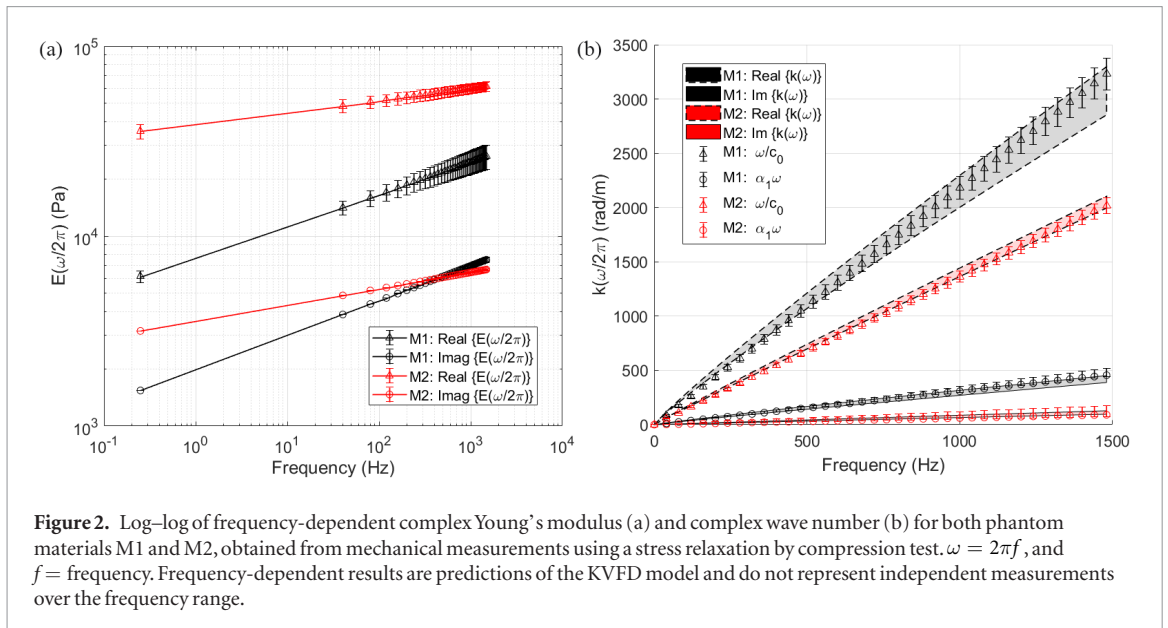
For the analysis, two tissue-mimicking phantoms were selected and used in EXP. A lossy viscoelastic phantom material M1 (model no. 16410001, CIRS, Inc., Norfolk, VA, USA), and a lossless aqueous viscoelastic phantom material M2 (Aquaflex US del pad, Parker Laboratories Inc., Fairfield, NJ, USA). The frequency-dependent Young's modulus of each phantom was measured using a stress-relaxation by compression test. The measurement was conducted using a MTS Q-Test/5 Universal Testing Machine (MTS, Eden Prairie, MN, USA) with a 5 N load cell using a compression rate of 0.5 mm s $^{-1}$, a strain value of 5%, and total measurement time of 600 s. The stress-time plots obtained by the machine were fitted to a three parameter Kelvin–Voigt fractional derivative (KVFD) model (Zhang *et al* 2008) for the calculation of frequency-dependent complex Young's modulus given as

$$\hat{E}(\omega) = \left[E_0 + \eta \cos\left(\frac{\pi\tau}{2}\right) \omega^\tau \right] + i \left[\eta \sin\left(\frac{\pi\tau}{2}\right) \omega^\tau \right], \quad (24)$$

where E_0 is the relaxed elastic constant, η is the viscous parameter, and τ is the order of fractional derivative. $\hat{E}(\omega)$ has the same form as $\hat{\mu}(\omega)$, and $\hat{E}(\omega) = E_s(\omega) + iE_l(\omega)$, where $E_s(\omega)$ and $E_l(\omega)$ are called the Young's storage and loss moduli, respectively. Measurements were conducted in three samples of each phantom type in order to calculate the mean and standard deviation (error) for each predicted frequency-dependent result. Estimations of the three parameters of the KVFD model for phantom materials M1 and M2 (table 1) are used to calculate the real and imaginary part of equation (24), plotted versus frequency in figure 2(a). Then, for a nearly incompressible (Poisson's ratio close to 0.5), homogeneous, and isotropic medium, the complex velocity of the shear wave for each phantom with a material density of ρ can be calculated (Parker *et al* 2011) as $\hat{c}(\omega) = \sqrt{\hat{\mu}(\omega)/\rho} = \sqrt{\hat{E}(\omega)/(3\rho)}$, and the complex wave number of equation (16) can be expressed as

$$\hat{k}(\omega) = \frac{\omega}{\hat{c}(\omega)} = \left[\frac{\omega}{\sqrt{2/(3\rho)}} \frac{\sqrt{|\hat{E}| + E_s}}{|\hat{E}|} \right] - i \left[\frac{\omega}{\sqrt{2/(3\rho)}} \frac{\sqrt{|\hat{E}| - E_s}}{|\hat{E}|} \right], \quad (25)$$

where $E_s = \text{Real}\{\hat{E}\}$ (see appendix B for details of the derivation). For both phantom materials, $\rho = 1 \text{ g cm}^{-3}$. The complex wave number from equation (25) is plotted in figure 2. Herein, c_0 and α_1 are estimated by fitting $\text{Real}\{\hat{k}(\omega)\}$ to ω/c_0 , and $\text{Im}\{\hat{k}(\omega)\}$ to $\omega\alpha_1$, respectively, over a frequency range from 0 Hz to 1500 Hz. Both components, ω/c_0 and $\omega\alpha_1$, come from the Taylor approximation of \hat{k} described in equation (17) and are estimated for both phantom materials M1 and M2 (table 1).



3.2. Numerical integration (NI)

Given equation (23), calculations of space-time representations of particle velocity $v_z(x, t)$ for a Gaussian-shape force ($\sigma = 0.338$ mm) and $g(t) = \delta(t)$ are performed using NI in MATLAB (The MathWorks, Inc. Natick, MA, USA). Radial spatial (r) and temporal (t) variables are set to range $[-4.5; 4.5]$ mm (200 samples), and $[0; 5]$ ms (400 samples), respectively. c_0 and α_1 are chosen from table 1 for M1, and M2, accordingly. Then, equation (15) is used to convolve results provided by equation (23) (impulse response) with $g(t)$, for the following cases: (1) phantom material M1, temporal rectangular pulse $g(t) = \text{rect}(\frac{t}{\tau_{M1,2}} - \frac{1}{2})$, with $\tau_{M1} = 1$ ms, and (2) phantom material M2, temporal rectangular pulse of $\tau_{M2} = 0.1$ ms.

3.3. Finite element simulation

Numerical simulations of shear wave propagation under an axisymmetric Gaussian force were conducted using FE in Abaqus/CAE version 6.14-1 (Dassault Systems, Vélizy-Villacoublay, France). A 2D axisymmetric deformable part was created and subjected to a Gaussian distribution body force with $\sigma = 0.338$ mm along the symmetry line (see figure 3). The outer vertical border was subjected to encastre boundary conditions (zero displacement and rotation). The model was meshed using approximately 13 280 hybrid, linear and quadrilateral-dominant elements (CAX4RH). Time domain viscoelastic material properties were chosen to characterize phantom materials M1 and M2, which are shown in table 2 together with the selected density and Poisson's ratio. Frequency-dependent Young's modulus extracted from mechanical measurements in section 3.1 (figure 2(a)) for M1 and M2 were provided as tabular data: $\omega R(h^*) = E_l/E_\infty$, and $\omega I(h^*) = 1 - E_s/E_\infty$, as function of $f = \omega/2\pi$, where E_∞ is the long-term Young's modulus, also known as the quasi-static Young's modulus $E_s(\omega \approx 0)$. For the analysis, E_∞ is considered E_0 (table 1). The details on $\omega R(h^*)$ and $\omega I(h^*)$ parameters required by Abaqus/CAE for the viscoelastic material definition are explained in appendix C.

The type of simulation was selected to be dynamic-implicit for a time range of 15 ms in order to let the shear waves propagate along the medium without producing reflections from the outer boundaries. Similarly, as in section 3.2, two sets of simulation were conducted: (1) phantom material M1, temporal rectangular pulse $g(t) = \text{rect}(\frac{t}{\tau_{M1,2}} - \frac{1}{2})$, with $\tau_{M1} = 1$ ms, and (2) phantom material M2, temporal rectangular pulse of $\tau_{M2} = 0.1$ ms. For both cases, the body force distribution was set to be $F_z(r) = A_0 (\frac{1}{2\sigma^2}) e^{-(\frac{r}{\sigma})^2}$, with $\sigma = 0.338$ mm. Space-time representations of particle velocity $v_{z_0}(r, t)$ were calculated in both cases at depth z_0 crossing through the middle of the medium along the xy -plane.

3.4. Experimental setup and acquisition

The experimental setup is shown in figure 4(a). A 5 MHz confocal ultrasonic transducer (PIM7550-2inchFL, Dakota Ultrasonics, Scotts Valley, CA, USA) with 5.01 cm of focal length was excited with a $\tau = \{0.1, 1\}$ ms sinusoidal tone of 5 MHz provided by a function generator (AFG320, Tektronix, Beaverton, OR, USA), representing shorter and longer acoustic push pulses. The generator was connected to a RF power amplifier (25A250, Amplifier Research, Souderton, PA, USA) in order to produce an approximate Gaussian, radially symmetric ($\sigma = 0.338$ mm) focused ARF push within the phantom up to the air-solid surface interface of the phantom. The ultrasonic transducer was coupled to the sample with saline water as shown in figure 3(b). A phase-sensitive optical coherence tomography (PhS-OCT) system implemented with a swept source laser

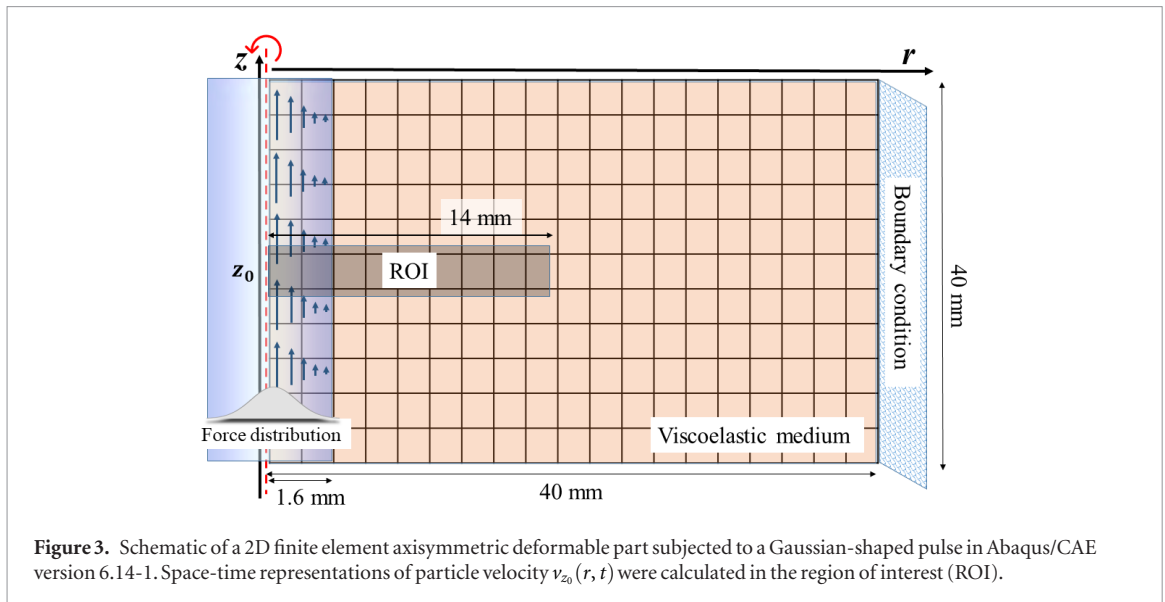
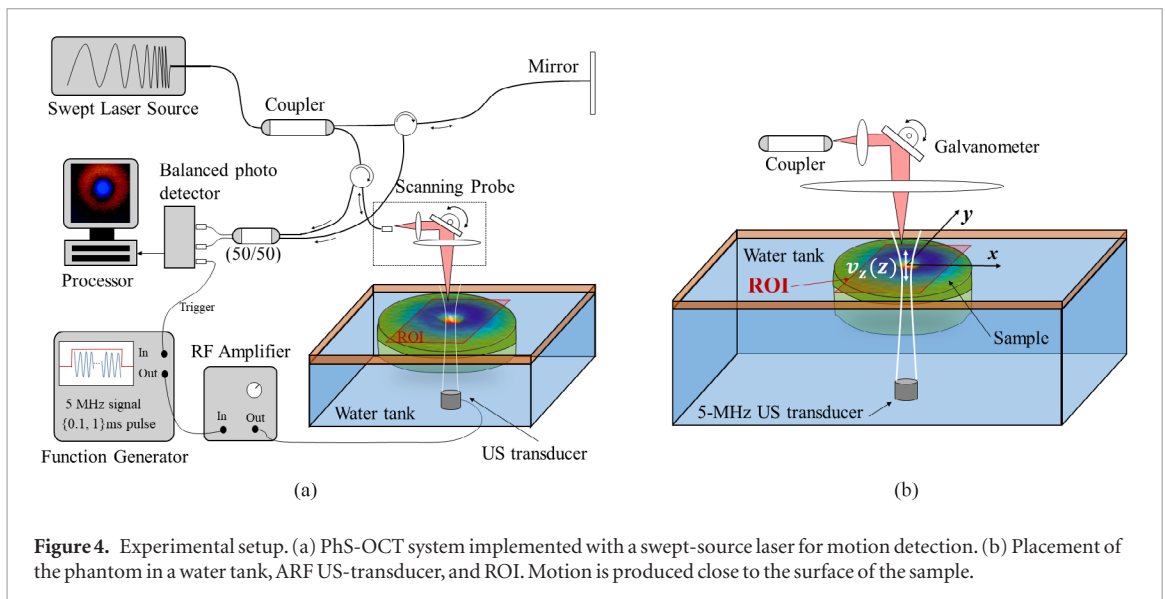


Table 2. Viscoelastic material parameters of phantom materials M1 and M2 in Abaqus/CAE version 6.14-1. The frequency-dependent parameters for each material were provided as tabular data: $\omega R(h^*) = E_l/E_\infty$, and $\omega I(h^*) = 1 - E_s/E_\infty$, as function of $f = \omega/2\pi$, where E_∞ is the long-term Young's modulus.

	Density, ρ (kg m^{-3})	Poisson's ratio, ν	Long-term Young's modulus, E_∞ (kPa)	Frequency-dependent tabular parameters	
				$\omega R\{h^*\}$	$\omega I\{h^*\}$
M1	998	0.499	0.711	E_l/E_∞	$1 - E_s/E_\infty$
M2	998	0.499	9.969		

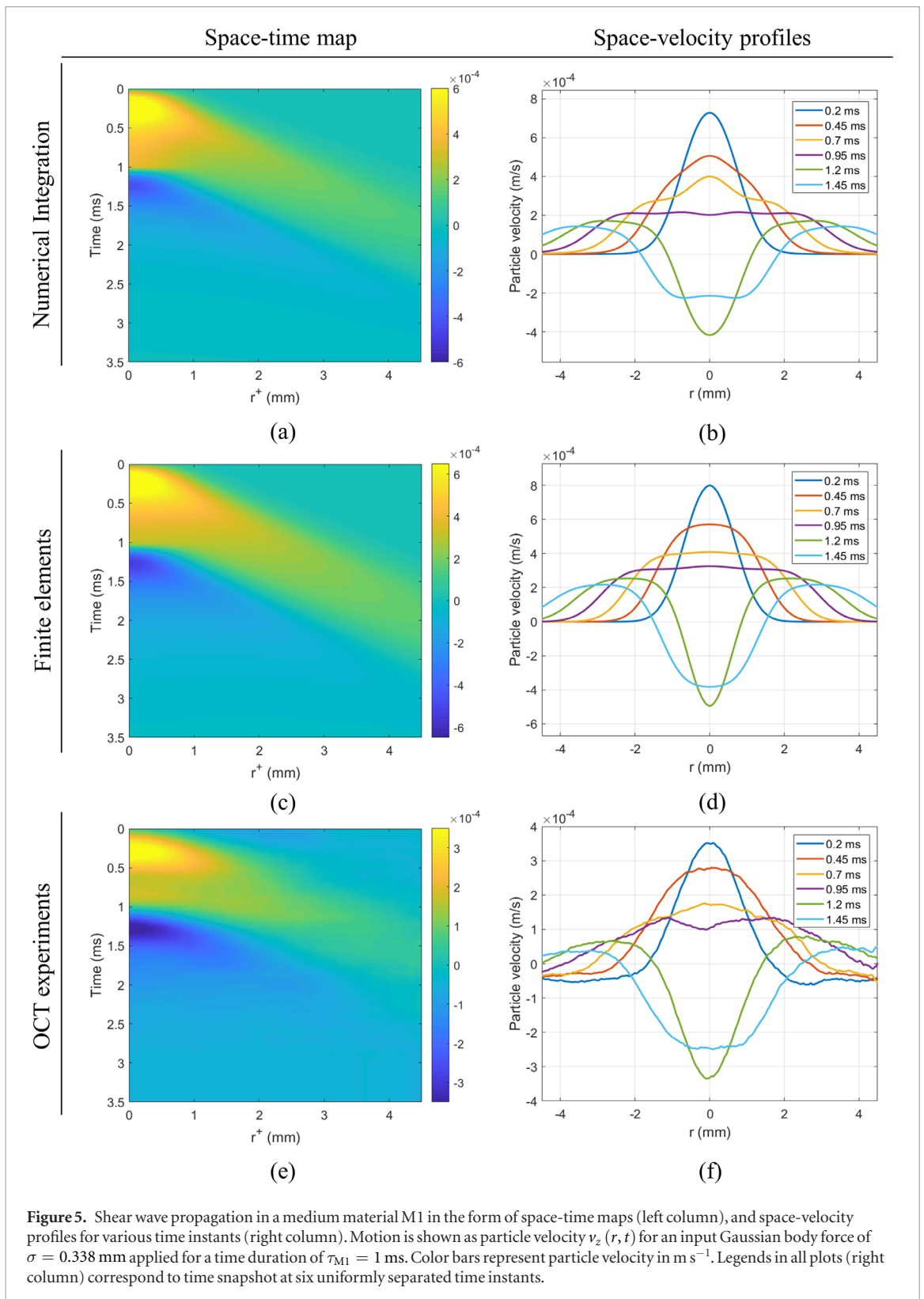


(HSL-2100-WR, Santec, Aichi, Japan) with a center wavelength of 1318 nm was used to acquire 3D motion (particle velocity) frames of the sample within a ROI of 9×9 mm in the xy -plane, at a depth $z_0 = 2$ mm in the z -plane. The OCT acquisition and the excitation of the 5 MHz transducer were triggered by the computer controlling the entire process. Details of the OCT system are provided in appendix D.

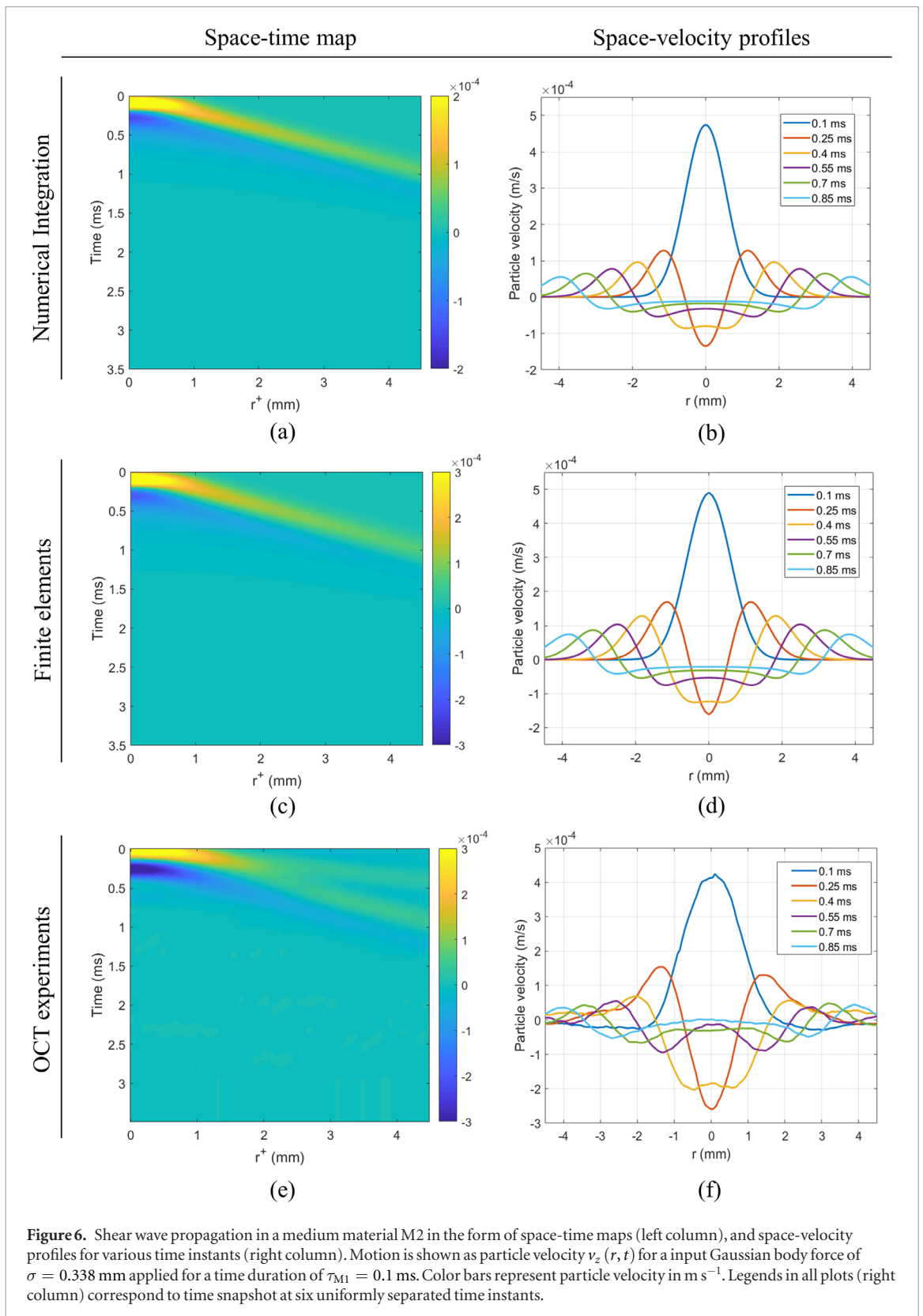
The ARF push was focused at a certain (x_0, y_0) position in the sample's surface (figure 4(b)), and it produced a localized out-of-plane vertical displacement that generated a cylindrically-shaped Rayleigh wave propagating within the ROI (Zvietcovich *et al* 2016). The relationship between shear wave and Rayleigh wave phase speed in a linear isotropic medium for a Poisson's ratio $\nu \approx 0.5$ is given by (Viktorov 2013)

$$c \approx 1.05 * c_{\text{Rayleigh}}. \quad (26)$$

For all cases, we used equation (26) to correct Rayleigh wave speed to shear wave speed.



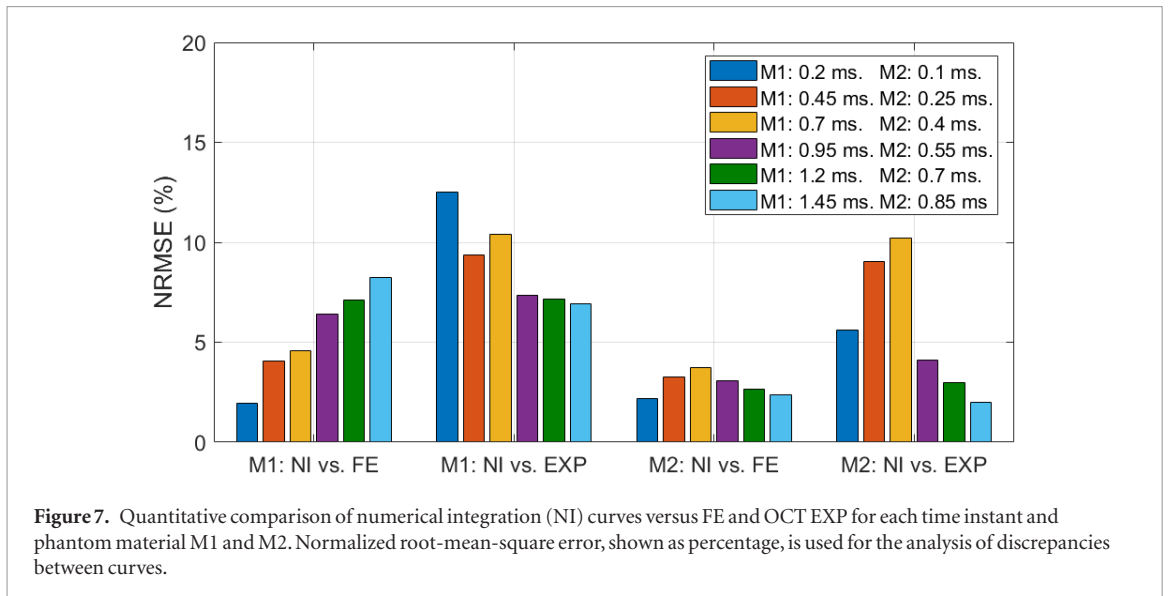
The M-B mode acquisition approach, as described in Zvietcovich *et al* (2017b), is used for generating x -axis space-time representations of particle velocity $v_{z_0}(x, t)$ at the given depth $z_0 = 2$ mm crossing the center of the ARF excitation (x_0, y_0) . Then, $v_{z_0}(x, t)$ is equivalent to $v_{z_0}(r, t)$ in cylindrical coordinates due to the axisymmetric shape of the force. Each space-time representation spans 200 locations in the x -axis (9 mm), and $M = 100$ time samples (5 ms). To reduce noise, experimental results for both M1 and M2 cases were subjected to a local regression filtering approach using weighted linear least squares and a 1st degree polynomial model with a kernel size of 10% of the time signal size. Two cases are analyzed using the proposed experimental setup: (1) phantom material



M1, temporal rectangular pulse $g(t) = \text{rect}(\frac{t}{\tau_{M1,2}} - \frac{1}{2})$, with $\tau_{M1} = 1$ ms, and (2) phantom material M2, temporal rectangular pulse of $\tau_{M2} = 0.1$ ms.

4. Results

Wave propagation results were evaluated using parameters provided in table 1 for the proposed material M1 and M2 in three cases: (1) NI using the proposed forward model, (2) simulations using FE in Abaqus/CAE, and (3) EXP in phantoms using an OCT imaging system. Particle velocity $v_z(r, t)$ is displayed in the form of space-



time maps (left column), and space-velocity profiles for various time instants (right column) in figures 5 and 6 for material M1, and M2, respectively. In all cases, the applied body force has a Gaussian shape described in equation (2) with a fixed $\sigma = 0.338$ mm. The time application of the body force is set to be a rect function starting at $t = 0$ s and a duration of $\tau_{M1} = 1$ ms for M1 (figure 5), and $\tau_{M2} = 0.1$ ms for M2 (figure 6). Normalized root-mean-square error (NRMSE), expressed as a percentage, is computed in curves provided by simulations and EXP, taking curves obtained using NI as reference, for each phantom material case for further comparison as shown in figure 7.

5. Discussion

A good agreement in wave propagation profiles between NI of the proposed forward model, simulations using FE, and EXP in phantoms demonstrate the validity of our approach for two types of viscoelastic material excited by the same Gaussian-shaped force applied at two different duration times. However, a perfect match between the three cases is not expected for a number of reasons (see figure 7). First, the proposed forward model assumes negligible dispersion: $c_p(\omega) \cong c_0$, and a first order Taylor approximation of attenuation $\alpha(\omega) = \alpha_1\omega$ which constrains our model to a frequency band that satisfies those conditions. In addition, simulations using FE are conducted using frequency-dependent material properties provided by mechanical testing and a rheological model. Although the appropriateness of using a KVFD model to describe the material behavior of M1 and M2 has been demonstrated by the higher fitting quality (0.999) compared with other rheological models (Voigt, Kelvin–Voigt, Zener Standard Linear Solid, and Standard Linear Solid Fractional Derivative), the standard error of the measurements during mechanical testing can be relevant for the comparison at higher frequencies (see figure 2(b)). Finally, when experimental results are compared to our approach, a scaling factor of $\frac{1}{2}$ is found between figures 5(b) and (f) for the M1 case, and a scale factor of $\frac{7}{8}$ is found between figures 6(b) and (f) for M2. Particle velocity data in phantoms using an OCT imaging system are obtained only a few millimeters below the surface of the phantom. Although we applied the Rayleigh-to-shear speed correction (equation (26)), other surface wave properties such as non-zero particle velocity in the r -direction can be pointed to as an experimental source of disagreement.

Other limitations of this study include the imprecise knowledge of the experimental parameters related to the beam pattern and the viscoelastic materials, and the limited number of cases in the study. A larger range of beam widths and viscoelastic materials will be required to more carefully determine the limits of applicability of the model. Furthermore, the theory applies to homogeneous and isotropic materials. Strongly anisotropic tissues such as muscle will require additional analyses.

6. Conclusion

The proposed forward model, under axisymmetric source conditions and the other negligible dispersion assumptions, offers a convenient compromise between simplicity and accuracy by avoiding the complex Hankel function with a singularity at the origin, by using two material parameters to characterize viscoelastic media and performing one NI of a simple function. Summarizing our findings, for an axisymmetric intensity force source $F_z(r)$ applied during an impulsive time, the shear wave particle velocity pattern can be expressed as either a spatial or a temporal transform.

$$v_z(r, t) = \frac{1}{2} \int_0^\infty \varepsilon \cdot \widehat{F}(\varepsilon) \cdot J_0(\varepsilon r) \cos(c\varepsilon t) d\varepsilon \quad (27)$$

or

$$v_z(r, t) = \int_0^\infty \omega \cdot \widehat{F}\left(\frac{\omega}{c}\right) \cdot J_0\left(\frac{\omega}{c} \cdot r\right) \cos(\omega t) d\omega \quad (28)$$

for an elastic medium. For a viscoelastic and weakly attenuating medium with negligible dispersion, the shear wave particle velocity pattern is expressed as

$$v_z(r, t) = \frac{1}{2} \int_0^\infty \varepsilon \cdot \widehat{F}(\varepsilon) \cdot J_0(\varepsilon r) \cos(c_0 \varepsilon t) e^{-\varepsilon c_0^2 \alpha_1 t} d\varepsilon \quad (29)$$

or

$$v_z(r, t) = \int_0^\infty \omega \widehat{F}\left(\frac{\omega}{c_0}\right) J_0\left(\frac{\omega}{c_0} r\right) \cos(\omega t) e^{-\alpha_1 \omega r} d\omega. \quad (30)$$

Furthermore, the form of the key equations (12) and (23) can be interpreted as the inverse Hankel transform of zeroth order of a modulated source term. As such, there are a number of efficient algorithms associated with the discrete Hankel transform that can be applied (Johnson 1987). Therefore, the proposed model can be efficiently implemented without the need for treating singularities of the $H_0^{(2)}$ Green's function, or excluding the source region. As such, these are useful for inverse-fitting problems in order to estimate c_0 and α_1 of a selected material based on the particle velocity space-time propagation plots. In addition, the model can be tailored to any other force application time $g(t)$ by performing the simple convolution described in equation (15). Future work will concentrate on extending this model for non-axisymmetric conditions, and validating it for the study of skin conditions, liver fibrosis, and corneal keratoconus.

Acknowledgments

The instrumentation engineering development of this research benefited from support of the II–VI Foundation. This work was supported by the National Institute of Health (NIH) grant number R21EB025290 and the Hajim School of Engineering and Applied Sciences at the University of Rochester. Fernando Zvietcovich is supported by Fondo para la Innovacion, la Ciencia y la Tecnologia FINCyT 097-FINCyT-BDE-2014 (Peruvian Government). Prof. Baddour was supported by the Natural Sciences and Engineering Research Council of Canada (RGPIN-2016-04190).

Appendix A

Here, we demonstrate the dual nature of the attenuated integral formulas from this derivation and an earlier approach by Parker and Baddour (2014). In this earlier work, under the assumption of first order dispersion (i.e. $c \cong c_0 + c_1 \omega$) and some approximate simplifications of the Hankel function of complex arguments, their equation (43) is re-written here for a Gaussian function as

$$u_z(r, \omega) \cong -A_0 \frac{\pi i}{2} e^{-\alpha_1 |\omega| r} H_0^{(2)} \left(\left[\frac{\omega}{c_0} - \left(\frac{\omega}{c_0} \right)^2 c_1 \text{sign}(\omega) \right] r \right) e^{-\sigma \left(\frac{\omega}{c_0} \right)^2}. \quad (A.1)$$

Now, if we apply the small dispersion assumption, then $c \cong c_0$, and $c_1 = 0$, and calculate particle velocity $v_z(r, \omega) = i\omega u_z(r, \omega)$, we find:

$$v_z(r, \omega) \cong A_0 \frac{\pi}{2} \omega e^{-\alpha_1 |\omega| r} H_0^{(2)} \left(\frac{\omega}{c_0} r \right) e^{-\sigma \left(\frac{\omega}{c_0} \right)^2}. \quad (A.2)$$

Using the general constraint for real and causal functions in the inverse Fourier transform (equation (23) from Parker and Baddour 2014), expanding the $H_0^{(2)}$ function into its Y_0 and J_0 components, and then identifying the J_0 function as the real part of this Fourier integrand, we find:

$$v_z(r, t) \cong A_0 \int_0^\infty \omega e^{-\alpha_1 \omega r} H_0^{(2)} \left(\frac{\omega}{c_0} r \right) e^{-\sigma \left(\frac{\omega}{c_0} \right)^2} \cos(\omega t) d\omega, \quad (A.3)$$

which appears identical to equation (23) when substituting ε for ω/c_0 , the constant A_0 is scaled by $2c^2$, and the attenuation term $e^{-\varepsilon c_0^2 \alpha_1 t}$ is replaced by $e^{-\alpha_1 |\omega| r}$ in equation (23). This duality has been described before by

Blackstock (2000) where the attenuation of propagating waves can alternatively and equivalently be assigned either as a function of space or time.

Appendix B

As explained in section 3.1, the derivation of equation (25) is conducted by assuming a complex Young's modulus $\hat{E}(\omega) = E_s(\omega) + iE_l(\omega)$, and a nearly incompressible (Poisson's ratio close to 0.5), homogeneous, and isotropic medium, where the complex velocity of the shear wave is described as $\hat{c}(\omega) = \sqrt{\hat{\mu}(\omega)/\rho} = \sqrt{\hat{E}(\omega)/(3\rho)}$. Then, the complex wave number can be expressed as:

$$\hat{k}(\omega) = \frac{\omega}{\hat{c}(\omega)} = \frac{\omega\sqrt{3\rho}}{\sqrt{\hat{E}}} = \frac{\omega\sqrt{3\rho}\sqrt{\hat{E}^*}}{\sqrt{\hat{E}}\sqrt{\hat{E}^*}} = \frac{\omega\sqrt{3\rho}\sqrt{\hat{E}^*}}{|\hat{E}|} \quad (\text{B.1})$$

where \hat{E}^* is the complex conjugate of \hat{E} , and $|\hat{E}|$ is the modulus of \hat{E} . Then, using identity 3.7.27 (Abramowitz and Stegun 1965), $\sqrt{\hat{E}^*}$ can be represented as

$$\sqrt{\hat{E}^*} = \sqrt{\frac{|\hat{E}| + E_s}{2}} - i\sqrt{\frac{|\hat{E}| - E_s}{2}}. \quad (\text{B.2})$$

Substituting equation (B.2) into (B.1) we have:

$$\hat{k}(\omega) = \omega\sqrt{\frac{3\rho}{2}} \left(\frac{\sqrt{|\hat{E}| + E_s}}{|\hat{E}|} - i\frac{\sqrt{|\hat{E}| - E_s}}{|\hat{E}|} \right)$$

which is equivalent to equation (25) in the manuscript.

Appendix C

In Abaqus/CAE, the viscoelastic behavior of material can be defined in tabular form by giving real and imaginary parts of $\omega g^*(\omega)$. As defined in the 22.7.2 section of the Abaqus user manual (ABAQUS/CAE 6.14 User's Manual, Online Documentation Help: Dassault Systèmes), $g^*(\omega)$ is the Fourier transform of the non-dimensional shear relaxation function $g(t) = \frac{G_R(t)}{G_\infty} - 1$, where $G_R(t)$ is the time-dependent shear relaxation modulus, and $\omega = 2\pi f$ is the angular frequency. Then, $\omega R(g^*) = G_l/G_\infty$, and $\omega I(g^*) = 1 - G_s/G_\infty$, where $R(\cdot)$ and $I(\cdot)$ are the real and imaginary part operators, respectively, and the complex shear modulus is defined as $\hat{G}(\omega) = G_s(\omega) + iG_l(\omega)$. Subscripts s and l refer to the storage and loss moduli, respectively. Since we are assuming a nearly incompressible material, $\hat{G}(\omega) = \hat{E}(\omega)/2$, and we can redefine the tabular parameters as $\omega R(h^*) = E_l/E_\infty$ and $\omega I(h^*) = 1 - E_s/E_\infty$, where the complex Young's modulus is defined as $\hat{E}(\omega) = E_s(\omega) + iE_l(\omega)$. We have changed the notation from g^* to h^* to stress the change to Young's modulus and avoid confusion with the previously defined $g(t)$ in the manuscript as the temporal application of force. Finally, the tabular form $\omega R(h^*)$ and $\omega I(h^*)$ parameters can be provided to Abaqus as a function of $f = \omega/2\pi$, since E_s , E_l , and E_∞ are already obtained from mechanical measurements (section 3.1).

Appendix D

The PhS-OCT characteristics include a full-width half-maximum (FWHM) bandwidth of 125 nm, and a light source frequency sweep rate of 20 kHz. The source power that entered the OCT interferometer was split by a 10/90 fiber coupler into the reference and sample arms, respectively. In the reference arm, a custom Fourier domain optical delay line was used for dispersion compensation. In the sample arm, a collimated light beam diameter of 6.7 mm at $1/e^2$ was directed onto a test phantom by a focusing imaging lens (LSM05, Thorlabs Inc., Newton, NJ, USA), coupled with a galvanometer scanning mirror placed at the front focal plane of the imaging lens to achieve telecentric scanning. The back-scattered light from the sample was recombined with the light reflected from the reference mirror with a 50/50 fiber coupler. The time-encoded spectral interference signal was detected by a balanced photo-detector (1817-FC, New Focus, CA, USA), and then digitized with a 500 Msamples/s, 12-bit-resolution analog-to-digital converter (ATS9350, AlazarTech, Pointe-Claire, QC, Canada). The maximum sensitivity of the system was measured to be 112 dB (Yao *et al* 2015). The imaging depth of the system was measured to be 5 mm in air (-10 dB sensitive fall-off). The optical lateral resolution

was approximately 30 μm , and the FWHM of the axial point spread function after dispersion compensation was 10 μm . The synchronized control of the galvanometer and the OCT data acquisition was conducted through a LabVIEW platform (National Instruments, Austin, TX, USA) connected to a workstation. The phase stability of the system was calculated as the standard deviation of the temporal fluctuations of the Doppler phase-shift ($\Delta\phi_{\text{err}}$) while imaging a static structure (Meemon et al 2010). Results show $\Delta\phi_{\text{err}} = 4.6$ mrad when using the Loupas' algorithm (Loupas et al 1995). The displacement sensitivity is measured as the minimum detectable axial particle displacement ($u_{z,\text{min}}$). We found $u_{z,\text{min}} = 0.358$ nm. Finally, the maximum axial displacement supported by the system without unwrapping the phase-shift signal ($\Delta\phi_{\text{max}} = \pi$) is $u_{z,\text{max}} = 0.24$ μm .

ORCID iDs

Natalie Baddour  <https://orcid.org/0000-0002-7025-7501>

Kevin Parker  <https://orcid.org/0000-0002-6313-6605>

References

- Abramowitz M and Stegun IA 1965 *Handbook of Mathematical Functions: With Formulas, Graphs, and Mathematical Tables* (New York: Dover)
- Baddour N 2011 Multidimensional wave field signal theory: mathematical foundations *AIP Adv.* **1** 022120
- Baddour N 2018 Addendum to foundations of multidimensional wave field signal theory: gaussian source function *AIP Adv.* **8** 025313
- Bercoff J, Tanter M and Fink M 2004 Supersonic shear imaging: a new technique for soft tissue elasticity mapping *IEEE Trans. Ultrason. Ferroelectr. Freq. Control* **51** 396–409
- Blackstock DT 2000 *Fundamentals of Physical Acoustics* (New York: Wiley)
- Carstensen E L and Parker K J 2014 Physical models of tissue in shear fields *Ultrasound Med. Biol.* **40** 655–74
- Fahey B J, Nightingale K R, McAleavey S A, Palmeri M L, Wolf P D and Trahey G E 2005 Acoustic radiation force impulse imaging of myocardial radiofrequency ablation: initial *in vivo* results *IEEE Trans. Ultrason. Ferroelectr. Freq. Control* **52** 631–41
- Graff K F 1975 *Wave Motion in Elastic Solids* (London: Oxford University Press)
- Johnson H F 1987 An improved method for computing a discrete Hankel transform *Comput. Phys. Commun.* **43** 181–202
- Kazemirad S, Bernard S, Hybois S, Tang A and Cloutier G 2016 Ultrasound shear wave viscoelastography: model-independent quantification of the complex shear modulus *IEEE Trans. Ultrason. Ferroelectr. Freq. Control* **63** 1399–408
- Leartrapun N, Iyer R and Adie S G 2017 Model-independent quantification of soft tissue viscoelasticity with dynamic optical coherence elastography *Proc. SPIE* **10053** 1005322
- Loupas T, Peterson R B and Gill R W 1995 Experimental evaluation of velocity and power estimation for ultrasound blood flow imaging, by means of a two-dimensional autocorrelation approach *IEEE Trans. Ultrason. Ferroelectr. Freq. Control* **42** 689–99
- Meemon P, Lee K-S and Rolland J P 2010 Doppler imaging with dual-detection full-range frequency domain optical coherence tomography *Biomed. Opt. Express* **1** 537–52
- Nenadic I Z, Qiang B, Urban M W, Zhao H, Sanchez W, Greenleaf J F and Chen S 2017 Attenuation measuring ultrasound shear wave elastography and *in vivo* application in post-transplant liver patients *Phys. Med. Biol.* **62** 484
- Nightingale K, Nightingale R, Palmeri M and Trahey G 1999 Finite element analysis of radiation force induced tissue motion with experimental validation *Paper Presented at the 1999 IEEE Ultrasonics Symposium. Proc. Int. Symp. (Cat. No.99CH37027)* (<https://doi.org/10.1109/ULTSYM.1999.849240>)
- Ophir J, Srinivasan S, Righetti R and ThittaiKumar A 2011 Elastography: a decade of progress *Curr. Med. Imaging Rev.* **7** 292–312
- Parker K J and Baddour N 2014 The Gaussian shear wave in a dispersive medium *Ultrasound Med. Biol.* **40** 675–84
- Parker K J, Doyley M M and Rubens D J 2011 Imaging the elastic properties of tissue: the 20 year perspective *Phys. Med. Biol.* **56** R1–29
- Parker K J, Ormachea J, Will S and Hah Z 2018 Analysis of transient shear wave in lossy media *Ultrasound Med. Biol.* **44** 1504–15
- Sarvazyan A P, Rudenko O V, Swanson S D, Fowlkes J B and Emelianov S Y 1998 Shear wave elasticity imaging: a new ultrasonic technology of medical diagnostics *Ultrasound Med. Biol.* **24** 1419–35
- Schmitt C, Hadj Henni A and Cloutier G 2010 Ultrasound dynamic micro-elastography applied to the viscoelastic characterization of soft tissues and arterial walls *Ultrasound Med. Biol.* **36** 1492–503
- Szabo T L 1995 Causal theories and data for acoustic attenuation obeying a frequency power law *J. Acoust. Soc. Am.* **97** 14–24
- Vappou J, Malek C and Konofagou E E 2009 Quantitative viscoelastic parameters measured by harmonic motion imaging *Phys. Med. Biol.* **54** 3579
- Viktorov I A 2013 *Rayleigh and Lamb Waves: Physical Theory and Applications* (Berlin: Springer)
- Wijesinghe P, McLaughlin R A, Sampson D D and Kennedy B F 2015 Parametric imaging of viscoelasticity using optical coherence elastography *Phys. Med. Biol.* **60** 2293
- Yao J, Meemon P, Ponting M and Rolland J P 2015 Angular scan optical coherence tomography imaging and metrology of spherical gradient refractive index preforms *Opt. Express* **23** 6428–43
- Zhang M, Nigwekar P, Castaneda B, Hoyt K, Joseph J V, di Sant' Agnese A and Parker K J 2008 Quantitative characterization of viscoelastic properties of human prostate correlated with histology *Ultrasound Med. Biol.* **34** 1033–42
- Zvietcovich F, Rolland J P and Parker K J 2017a An approach to viscoelastic characterization of dispersive media by inversion of a general wave propagation model *J. Innov. Opt. Health Sci.* **10** 1742008
- Zvietcovich F, Rolland J P, Yao J, Meemon P and Parker K J 2017b Comparative study of shear wave-based elastography techniques in optical coherence tomography *J. Biomed. Opt.* **22** 035010
- Zvietcovich F, Yao J, Rolland J P and Parker K J 2016 Experimental classification of surface waves in optical coherence elastography *Proc. SPIE* **9710** 97100Z